ISPRS Open Journal of Photogrammetry and Remote Sensing 10 (2023) 100047

Contents lists available at ScienceDirect

ISPRS Open Journal of Photogrammetry and Remote Sensing

journal homepage: www.journals.elsevier.com/isprs-open-journal-of-photogrammetry-and-remote-sensing

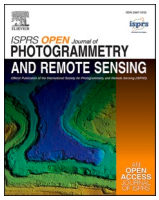

Pol-InSAR-Island - A benchmark dataset for multi-frequency Pol-InSAR data land cover classification

Sylvia Hochstuhl [a,b,*], Niklas Pfeffer [a,b], Antje Thiele [a,b], Stefan Hinz [a], Joel Amao-Oliva [c], Rolf Scheiber [c], Andreas Reigber [c], Holger Dirks [d]

[a] Institute of Photogrammetry and Remote Sensing, Karlsruhe Institute of Technology, Germany
[b] Fraunhofer IOSB, Ettlingen, Germany
[c] Microwaves and Radar Institute, German Aerospace Center (DLR), Wessling, Germany
[d] Lower Saxony Water Management, Coastal Defence and Nature Conservation Agency - Coastal Research Station, Norden, Germany

ARTICLE INFO

Keywords:
Pol-InSAR
Multi-frequency
Benchmark dataset
Land cover classification
Machine learning
Wishart classifier
Random forest classifier

ABSTRACT

This paper presents Pol-InSAR-Island, the first publicly available multi-frequency Polarimetric Interferometric Synthetic Aperture Radar (Pol-InSAR) dataset labeled with detailed land cover classes, which serves as a challenging benchmark dataset for land cover classification. In recent years, machine learning has become a powerful tool for remote sensing image analysis. While there are numerous large-scale benchmark datasets for training and evaluating machine learning models for the analysis of optical data, the availability of labeled SAR or, more specifically, Pol-InSAR data is very limited. The lack of labeled data for training, as well as for testing and comparing different approaches, hinders the rapid development of machine learning algorithms for Pol-InSAR image analysis. The Pol-InSAR-Island benchmark dataset presented in this paper aims to fill this gap. The dataset consists of Pol-InSAR data acquired in S- and L-band by DLR's airborne F-SAR system over the East Frisian island Baltrum. The interferometric image pairs are the result of a repeat-pass measurement with a time offset of several minutes. The image data are given as 6×6 coherency matrices in ground range on a 1 m $\times$ 1m grid. Pixel-accurate class labels, consisting of 12 different land cover classes, are generated in a semi-automatic process based on an existing biotope type map and visual interpretation of SAR and optical images. Fixed training and test subsets are defined to ensure the comparability of different approaches trained and tested prospectively on the Pol-InSAR-Island dataset. In addition to the dataset, results of supervised Wishart and Random Forest classifiers that achieve mean Intersection-over-Union scores between 24% and 67% are provided to serve as a baseline for future work. The dataset is provided via KITopenData: https://doi.org/10.35097/1700.

1. Introduction

For the observation of the constantly changing earth surface, Polarimetric Synthetic Aperture Radar (PolSAR) systems provide an important contribution. The active sensor technology, in which electromagnetic waves of different polarization are transmitted and received, enables the recording of information-rich data unaffected by cloud cover and daylight. By analyzing the backscattered signal and, in particular, its polarimetric properties, conclusions can be drawn about the geophysical parameters of observed surfaces and the geometry and orientation of objects on the ground. In the current development of effective methods for land cover classification of PolSAR images, attention is mainly focused on methods from the field of machine learning, especially on its subfield deep learning as summarized in (Zhu et al., 2021) and (Parikh et al., 2020). This trend is primarily motivated by the tremendous success of deep learning methods for the analysis of optical image data. While this success has been strongly driven by public benchmark datasets such as ImageNet (Deng et al., 2009) and CityScale (Cordts et al., 2016), which contain a large number of labeled training and test data, comparable datasets for the PolSAR domain are rare. Due to the inherent differences in imaging techniques, the use of models pre-trained on optical data is inappropriate for the analysis of PolSAR data. Therefore, models must be trained from scratch, which requires domain-specific datasets. The lack of highly demanded large and representative expert-labeled benchmark datasets for the SAR community is highlighted by Zhu et al. in (Zhu et al., 2021) in their analysis of

* Corresponding author. Institute of Photogrammetry and Remote Sensing, Karlsruhe Institute of Technology, Germany.
E-mail address: Sylvia.Hochstuhl@kit.edu (S. Hochstuhl).

https://doi.org/10.1016/j.ophoto.2023.100047
Received 26 June 2023; Received in revised form 25 September 2023; Accepted 25 September 2023

the current state of deep learning-based SAR image analysis.

Only few open PolSAR datasets labeled by land cover classes exist that are frequently used in the respective literature to evaluate approaches for land cover classification. These are:

- The Flevoland dataset, which contains a PolSAR image (1024 × 1024 pixels) acquired by the NASA/JPL AIRSAR system and ground truth data, in the form of 14 crop type classes. The ground truth was collected within the 1991 MAC-Europe campaign (Vissers and Sanden, 1992).
- The Oberpfaffenhofen E-SAR dataset,[1] which contains a PolSAR image (1300 × 1200 pixels) labeled with three land cover classes (*Built-up Area*, *Wood Land,* and *Open Area*).
- The PolSF dataset (Liu et al.), which contains PolSAR images (1024 × 900 to 2784 × 5056 pixels) from various spaceborne systems (Gaofen-3, RADARSAT-2, RISAR, ALOS2) and an airborne system (AIRSAR) over San Francisco alongside with different versions of land cover labels.
- The AIR-PolSAR-Seg (Wang et al., 2022) dataset, which contains a PolSAR image (9082 × 9805 pixels) acquired by the Gaofen-3 system and labeled by six land cover classes (*Natural*, *Water*, *Land Use*, *Industrial*, *Housing,* and *Others*).

The enumerated datasets, however, have several limitations that make them inadequate for evaluating machine learning classifiers. An inherent limitation of the Flevoland, Oberpfaffenhofen, and PolSF datasets is the absence of predefined training and test areas. This lack of standardization poses a significant challenge when attempting to compare research results across various studies. Another shortcoming is the lack of complexity of the provided classification task. For instance, the Oberpfaffenhofen dataset employs merely three easily distinguishable classes. The Flevoland dataset, on the other hand, consists of 14 distinct and inherently self-resembling classes. However, they are arranged rectangularly, which greatly simplifies the image segmentation. As a result, very high classification performance can already be achieved with simple classifiers for these datasets, making it not feasible to compare more sophisticated classifiers that are needed for tackling more challenging real-world tasks. The recently presented AIR-PolSAR-Seg (Wang et al., 2022) dataset represents an attempt to provide an open labeled large-scale PolSAR benchmark dataset with high scene complexity and, thus a more challenging land cover classification task. However, a major drawback of this dataset is that only amplitude images are available, and consequently, a significant part of the polarimetric information cannot be included in the classification.

Besides SAR polarimetry, SAR interferometry is a valuable and established remote sensing technique that provides complementary information about the surface topography and temporal variability of an observed area. The relevant information is contained in the phase difference between two complex-valued SAR images of the same scene acquired from slightly different look angles. The combination of polarimetry and interferometry, known as Pol-InSAR (Cloude and Papathanassiou, 1998), results in a powerful observation space that can further improve land cover classification as shown in (Lee et al., 2005; Shimoni et al., 2009; Schmitz et al., 2020). In addition, current airborne Pol-InSAR systems allow simultaneous acquisition in multiple frequency bands. This extends the observation space by an additional component that is beneficial in distinguishing land cover types, as shown in (Chen et al., 1996; Turkar et al., 2012; Schmitz et al., 2022a). The development of deep learning methods for single- and multi-frequency PolSAR classification has already achieved success and is actively pursued ((Xie et al., 2014; Gao et al., 2017; Zhang et al., 2017; De et al., 2018; Xin et al., 2022; Cao et al., 2023)). However, their application to the analysis of single- and especially multi-frequency Pol-InSAR data is very limited ((Mohammadimanesh et al., 2019; Newman et al., 2023; Wang and Wang, 2019)). The main reason for the scarce research activity in this area is certainly the very limited open access availability of Pol-InSAR data and the lack of labeled benchmark datasets for training and testing classifiers. To fill this gap and to advance the development of learning-based classification, this work presents a dataset called Pol-InSAR-Island, which provides multi-frequency Pol-InSAR data along with a challenging classification task consisting of 12 land cover classes. The difficulty of the classification task is mainly due to the focus on natural land cover classes, which are similar in appearance and continuously merge into each other. The dataset is intended to enable the training and fair comparison of different models for the classification of single- or multi-frequency PolSAR and Pol-InSAR data. All in all, the Pol-InSAR-Island dataset stands out from existing benchmark datasets due to the following advantages:

1. **Open provision of labeled multi-frequency Pol-InSAR data in high resolution**: Pol-InSAR-Island is the first open benchmark dataset for the classification of multi-frequency Pol-InSAR data.
2. **Challenging classification task due to high scene complexity**: The dataset comprises 12 different natural land cover classes characterized by high intra-class variance and inter-class similarity. Another challenge arises from the imbalance in the number of samples per class that is typical for real-world data.
3. **Controlled training and test setting**: In total, the dataset contains more than 5 million labeled pixels, which are equally divided into spatially disjoint training and test sets. When partitioning the dataset, care was taken to ensure similar class strengths between the training and test sets. For comparison, two common evaluation metrics, namely Intersection-over-Union (IoU) and balanced accuracy, are proposed.

The following content of this article is divided into four sections. First, in Section 2, the Pol-InSAR data, their properties, and their representation form are described, along with the process of class labeling based on reference data. In Section 3, classification results achieved by two established classifiers on the dataset are given that serve as baselines. Subsequently, in Section 4, the advantages and limitations of the presented dataset are discussed. Finally, the main components are summarized in Section 5.

2. Data basis and labeling

2.1. F-SAR data

The Pol-InSAR data of the Pol-InSAR-Island dataset were acquired over the German Wadden Sea in April 2022 on behalf of the Lower Saxony Water Management, Coastal Defence and Nature Conservation Agency (NLWKN). The measurement campaign was conducted with the airborne F-SAR system developed at the German Aerospace Center (DLR) (Horn et al., 2009). The captured area covers the islands Norderney, Baltrum, and Langeoog, including the surrounding tidal flat area. The Pol-InSAR-Island dataset does not contain all the SAR data acquired during the campaign but only the data segments covering the island of Baltrum. The reason for this is the high time effort required for quality-assured labeling of the land cover. The decision to initially focus on the island of Baltrum is due to the fact that a high diversity of land cover classes is available within a comparatively small area. As shown in Fig. 1, the selected data sections, each covering an area of 2.5 km × 3.6 km, originate from two overlapping flight paths, which were acquired in opposite flight directions. The incidence angle interval used to capture these sections ranges from 26 ° to 58 °. As described in (Horn et al., 2009), the F-SAR system allows the acquisition of fully polarimetric SAR data (S_{hh}, S_{vv}, S_{vh}, S_{hv}) in five frequency bands: P, L, S, C, and

[1] At the time of publishing this paper, unfortunately, the dataset is no longer available through the commonly referenced link: (https://earth.esa.int/web/polsarpro/data-sources/sample-datasets).

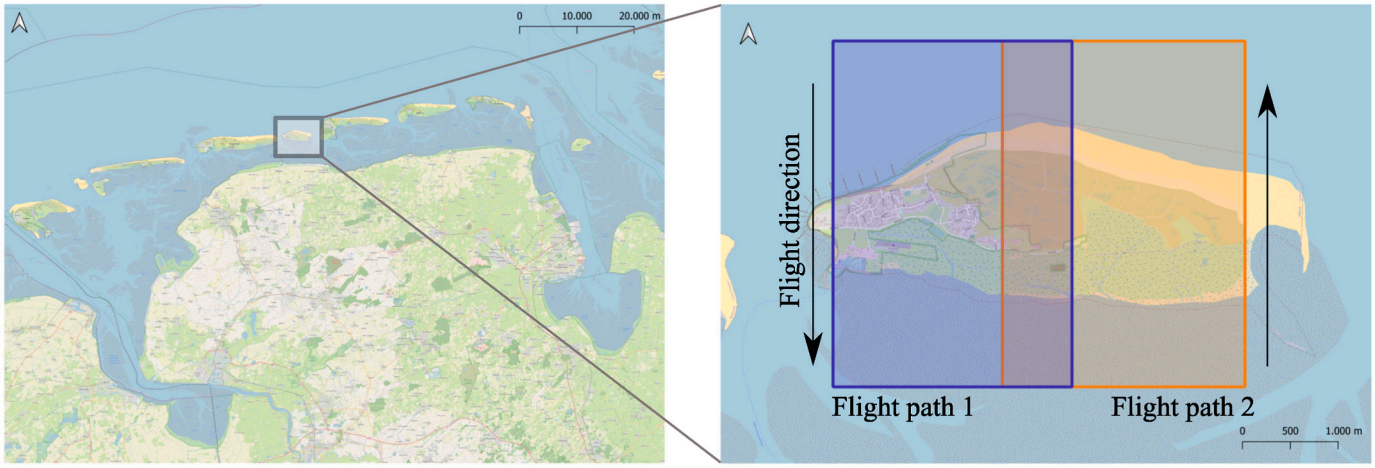

Fig. 1. Geographic location of the F-SAR measurement campaign 2022 and selected areas for the Pol-InSAR-Island dataset. The flight paths, shown in the right figure, were each captured twice using a vertical baseline of 40 m, a horizontal baseline of 0 m, and a time offset of 12 min.

X. The data considered for the Pol-InSAR-Island dataset were acquired simultaneously in S- and L-band, corresponding to frequencies of 3.25 GHz and 1.325 GHz, respectively. The resulting images have a resolution of 0.65 m (S) and 1.29 m (L) in range and 0.5 m (S) and 0.6 m (L) in azimuth. The interferometric analysis is enabled by imaging in a repeat-pass configuration, where the area was imaged twice with a time offset of 12 min, a nominal vertical baseline of 40 m, and a horizontal baseline of 0 m. Detailed information about the concepts of data acquisition and processing, which have been developed within the GeoWAM project (Pinheiro et al., 2021), can be found in (Pinheiro et al., 2020). Fig. 2 shows the multi-frequency Pol-InSAR imagery included in the Pol-InSAR-Island dataset in the form of color-coded images based on Pauli decomposition and interferometric coherences.

Based on co-registered single-look complex interferometric image pairs, the hermitian positive semi-definite coherency matrix $\mathbf{T}_6$ is calculated for each pixel. It is obtained from the scalar product of the scattering vectors k_1 and k_2 in Pauli basis:

$$\mathrm{k}_i = \frac{1}{\sqrt{2}}[S_{hh} + S_{vv}, S_{vv} - S_{hh}, 2S_{hv}]^T \tag{1}$$

$$\mathbf{T}_6 = \begin{bmatrix} \mathrm{k}_1 \\ \mathrm{k}_2 \end{bmatrix} \begin{bmatrix} \mathrm{k}_1^{*T} & \mathrm{k}_2^{*T} \end{bmatrix} = \begin{bmatrix} \mathbf{T}_{11} & \mathbf{\Omega}_{12} \\ \mathbf{\Omega}_{21} & \mathbf{T}_{22} \end{bmatrix}. \tag{2}$$

Here, * denotes the complex conjugation, and ^{T} stands for the matrix

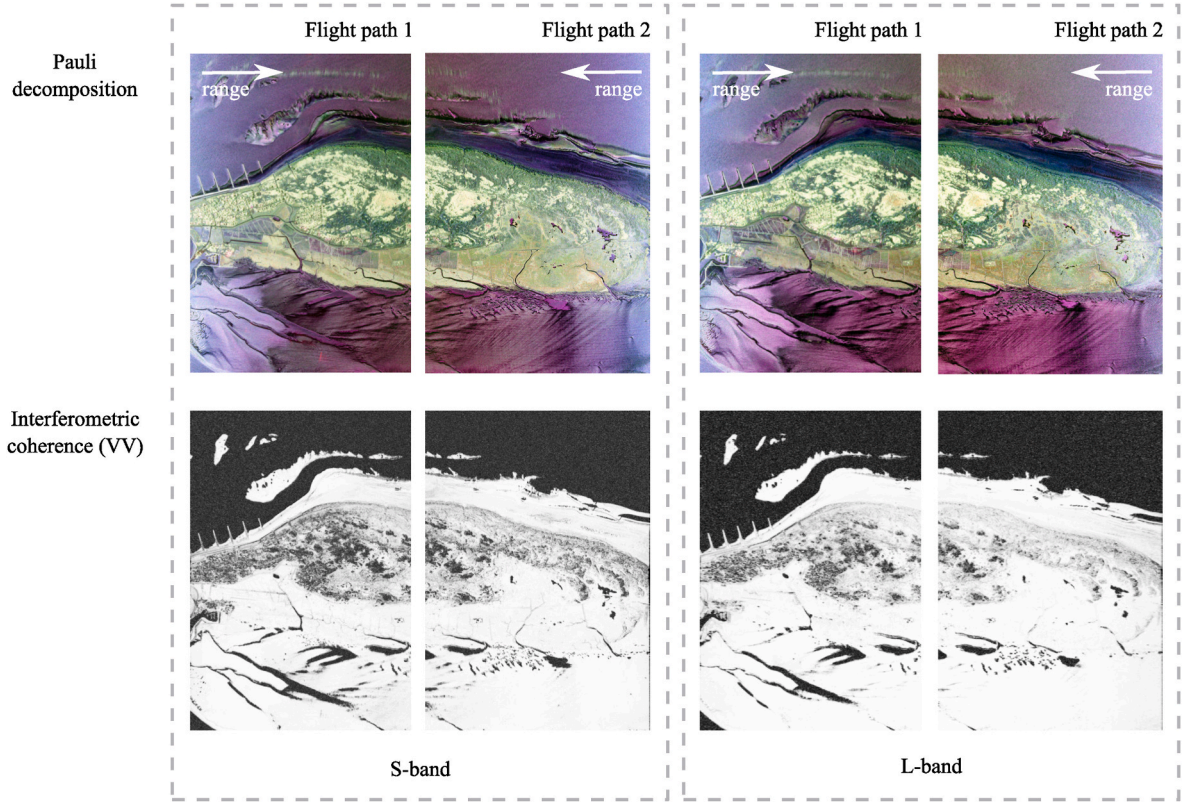

Fig. 2. Geocoded Pol-InSAR image data of the Pol-InSAR-Island dataset. The image data of both frequency bands are visualized by polarimetric composites (Pauli decomposition) and interferometric coherence in VV polarization.

transposition. The two matrices $\mathbf{T}_{11}$ and $\mathbf{T}_{22}$ represent the coherency matrices of the individual PolSAR images that contain polarimetric information. The interferometric information of all polarimetric channels, which is carried particularly in the phase difference between both images, is contained in the matrices $\mathbf{\Omega}_{12}$ and $\mathbf{\Omega}_{21}$. Spatial filtering, which is usually performed to statistically describe distributed scatterers and reduce speckle noise, is not performed at this point but is left to the users of the dataset. The only postprocessing step performed is the computation and removal of the flat-earth phase from the components in $\mathbf{\Omega}_{12}$ and $\mathbf{\Omega}_{21}$. Subsequently, the resulting representation is projected from the slant range to the ground range geometry on a 1 m $\times$ 1 m grid. In the Pol-InSAR-Island dataset, the geocoded image data, containing the $\mathbf{T}_6$ matrix for each pixel, are provided in S- and L-band. In addition, the dataset contains auxiliary files that map the incidence angle as well as the vertical wavenumber.

2.2. Reference data

The island of Baltrum is 6.5 km^2 in size and, thus, the smallest of the seven East Frisian Islands of Germany. The island faces the North Sea to the north, while to the south, there are tidal flats between the island and the mainland. These tidal flats form a unique ecosystem that is regularly flooded and drained again. The island itself is home to many different types of biotopes typical of North Sea islands. These include salt marshes, bogs, and dune valleys. In addition, part of the island is built up with settlements. Artificial coastal protection structures can be found in the northwestern coastal area. This diverse land cover results in the target classes of the demanding Pol-InSAR-Island dataset. To realize fine-grained labeling of the land cover with a high degree of semantic detail, an existing biotope type map is used, published by the Lower Saxon Wadden Sea National Park Authority (NLPV) and provided via the geodata portal Marine Dateninfrastruktur Niedersachsen (MDI-NI) (https://mdi.niedersachsen.de/). This biotope type map was generated in 2013 as part of the Trilateral Monitoring and Assessment Program (TMAP), which aims to provide a substantial basis for policy-making on the protection of the Wadden Sea ecosystem. In the map, the island of Baltrum is divided into 40 biotope types. The biotope type map is visualized in Fig. 3. Since the biotope type map was generated several years before the F-SAR measurement campaign, significant changes in the extent of the different biotopes are to be expected, making the map not sufficient for accurate labeling. Therefore, the map is revised within a semi-automatic process, which is schematically illustrated in Fig. 4.

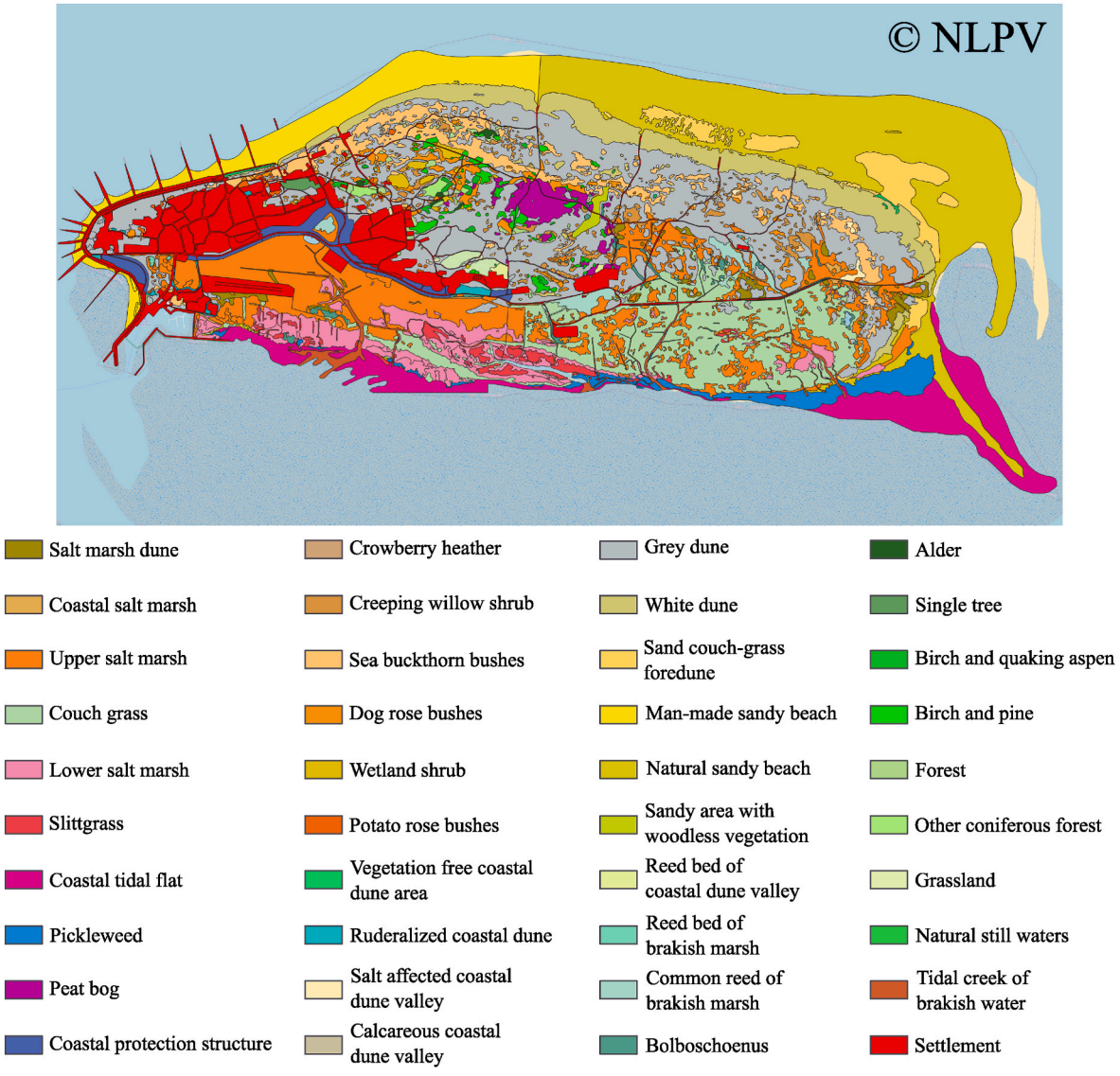

Fig. 3. Biotope type map (2013) of the island of Baltrum provided by MDI-NI.

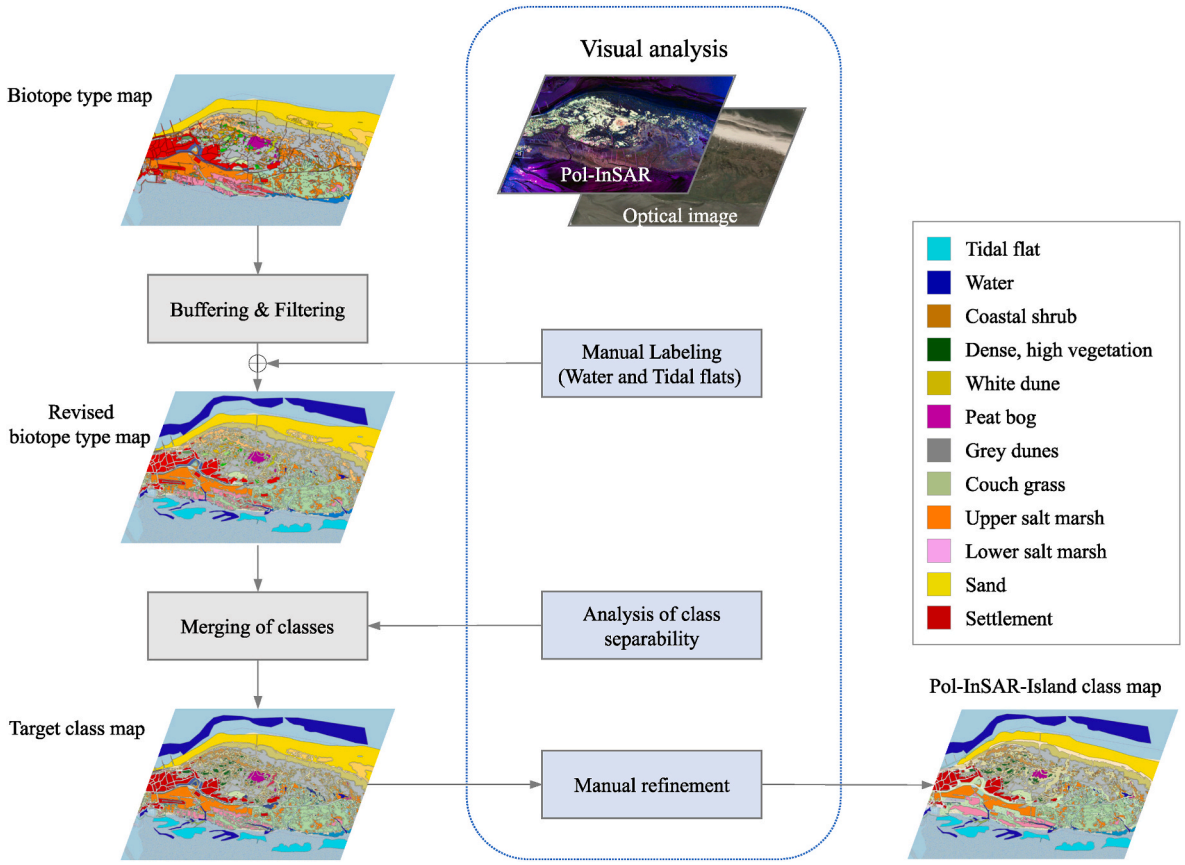

Fig. 4. Workflow of the semi-automatic process for data labeling.

2.2.1. *Revised biotope type map*

The biotope type map used as a starting point is given as a vector file, where each polygon contains exactly one biotope type attribute. The first step of the revision *Buffering & Filtering* aims at masking out areas where the class assignment of the outdated biotope type map is highly unlikely to match the land cover at the time of the SAR acquisition. It is assumed that this is particularly the case at transition areas of adjacent biotope boundaries. Moreover, the boundaries between two biotopes are usually fuzzy by nature, so an unambiguous class assignment is not possible. Therefore, all polygons of the biotope type map are adjusted with a negative buffer operation to shrink their extent and to create an empty space without an assigned biotope type between two different biotope types. Subsequently, biotope types that collectively cover less than 1000 m^2 over the complete study area are excluded from the dataset. Furthermore, areas that are assigned to the biotope type *Coastal tidal flat*, *Pickleweed*, or *Tidal creek of brackish water* are masked out. The reason for this approach is that the extent of exposed tidal flats is primarily determined by the current tidal phase, i.e., the current water level. Thus, the water level at the time of the SAR data acquisition can only be identified by interpreting the Pol-InSAR data itself. Therefore, a visual analysis of SAR backscatter amplitudes and interferometric coherences is performed to manually identify tidal flat areas and water areas that are added to the map. The resulting map is called the revised biotope type map.

2.2.2. *Target class map*

In the following processing step, *Merging of classes*, the original semantically fine-grained biotope types are grouped and assigned to generalized land cover classes, which form the final target classes of the benchmark dataset. The requirement for these target classes is that class separation using the multi-frequency Pol-InSAR data is possible but not trivial, so the dataset provides a challenging classification task. To determine an appropriate grouping of biotope types, a multi-stage visual class separability analysis is performed. This analysis is based on a visualization of the data structure of multi-frequency Pol-InSAR features. For this purpose, a 54-dimensional feature vector is generated for each pixel by stacking polarimetric and interferometric features listed in Table 1, that are extracted from S- and L-band data. The polarimetric features are computed based on the coherency matrix of the reference scene ($\mathbf{T_{11}}$). To visualize the high-dimensional feature representation of the data, an embedding in a 2-dimensional Euclidean space is computed using the dimension reduction method Uniform Manifold

Table 1
List of considered polarimetric and interferometric features.

Expression	Feature description
$T_{11,ij}$	Magnitude (in dB) and phase of the upper triangular elements of polarimetric coherency matrix $\mathbf{T}_{11}$
H, A, α	Entropy, anisotropy and mean alpha angle derived by eigenvalue decomposition (Cloude and Pottier, 1997)
p_1, p_2, p_3	Normalized eigenvalues of $\mathbf{T}_{11}$
$\bar{\lambda} = \sum_{i=1}^{3} p_i \lambda_i$	Weighted mean of eigenvalues
f_{odd}, f_{double}, f_{volume}	Contribution of scattering mechanisms to the total backscattered power derived by Yamaguchi decomposition (Yamaguchi et al., 2006)
Conformity coefficient	Conformity coefficient defined in (Truong-Loi et al., 2009)
Scattering diversity, scattering predominance, depolarization index, degree of purity	Parameters derived from the Frobenius Norm of the power-normalized coherency matrix (Praks et al., 2009)
$\lvert\gamma_{xx}\rvert$	Magnitude of interferometric coherence in VV, HV and HH polarization

Approximation and Projection (UMAP) (McInnes et al.). The UMAP algorithm aims at preserving local and global neighborhood relations of the data, which in the present application describe the similarity of the selected Pol-InSAR features. A resulting embedding of the multi-frequency Pol-InSAR data is shown in Fig. 5. Here, data points are colored according to their membership in one of six generic classes: *Tidal flat*, *Water*, *Dunes landscape*, *Salt marshes*, *Sand,* and *Settlement*. This class division was defined manually by grouping the specific biotope types based on their semantic meaning. The clustering observed in the scatterplot suggests a good separability of the six generic classes. While the classes *Tidal flat*, *Water*, *Sand,* and *Settlement* represent only one biotope type each, the classes *Dunes landscape* and *Salt marshes* are composed of many different biotope types, whose separability is further investigated. For this purpose, two additional embeddings are computed, in which only the pixels of the classes *Salt marshes* and *Dunes landscape* are included. The resulting embeddings are shown in Fig. 6. In the scatterplot, data points are colored based on their class as specified by the revised biotope type map. Note that reapplying the nondeterministic UMAP algorithm to the corresponding data subsets results in slight variations in the arrangement of data points in the 2-dimensional feature space. From the scatterplot corresponding to the class *Salt marshes*, separability of the biotope types *Couch grass* (light green) and *Upper salt marsh* (orange) can be derived. Another cluster is formed by the data points of the biotope types *Slit grass* and *Lower salt marsh*, which overlap strongly and are therefore combined into one target class *Lower salt marsh*. The generic class *Dunes landscape* is composed of 14 biotope types whose similarities with respect to their corresponding Pol-InSAR features are shown in the lower part of Fig. 6. The three biotope types, *White dune* (yellow), *Peat bog* (violet), and *Grey dune* (grey) stand out as distinct clusters. The remaining biotope types have similar Pol-InSAR features and, therefore, partially overlap in the 2-dimensional feature space. However, a separation between biotope types that can be assigned to the class *Dense, high vegetation,* and biotope types that can be assigned to the class *Coastal shrub* is possible. The presented analysis results in 12 target classes for the Pol-InSAR-Island dataset: *Tidal flat*, *Water*, *Coastal shrub*, *Dense and high vegetation*, *White dune*, *Peat bog*, *Grey dune*, *Couch grass*, *Upper salt marsh*, *Lower salt marsh*, *Sand* and *Settlement*. In Fig. 7, the feature representation of the entire dataset is shown, with the data points colored based on these 12 target classes. This figure gives a first impression regarding the degree of difficulty of class separation. A brief description of each target class is given below.

- *Tidal flats (TF)* are sandy, muddy areas that are repeatedly flooded and drained. They lie between the island and the mainland, and tideways are present during low tide periods. As they are regularly flooded, they are characterized by high moisture and little vegetation.
- *Water (W)* represents the North Sea, tideways running through the tidal flats, as well as waterways and small lakes located on the island.
- *Coastal shrub (CS)* represents low-growing shrubbery, such as sea-buckthorn, creeping willow, and potato rose bushes.
- *Dense, high vegetation (DV)* contains all the biotope types covering forested areas, as well as dense and high shrubbery.
- *White dune (WD)* represents areas with multiple meter-high dunes located next to the beach. They are covered by a more or less open low-growing vegetation cover of beach grass.
- *Peat bog (PB)* is the rarest class in the dataset and occurs as one large area in the center of the island Baltrum. It is a moist to swampy area covered by vegetation such as floodplains or creeping willow bushes.
- *Grey dune (GD)* represents a dune landscape which is covered with fireweed, thistles, or rubus.
- *Couch grass (CG)* identifies the fallow land of a formerly pastured upper salt marsh with couch grass dominance.
- *Upper salt marsh (US)* extends to about 70 cm above the high tide line and is flooded only 25–70 times per year. It is home to numerous plant species, including salt marsh red fescue, milkweed, beach mugwort, and beach quackgrass.
- *Lower salt marsh (LS)* extends to about 30 cm above the high tide line and is flooded 100–300 times per year. Prevalent species are andelgrass, beach aster, beach lilac, beach trident, and purslane wedgewort.
- *Sand (S)* covers the beach areas, as well as sandy areas without vegetation near dunes. *Sand* is mostly found in the western and northern areas of the island, facing the seaside.
- *Settlement (SE)* represents the major settlement area in the west of the island, as well as isolated buildings and settlements. No individual houses are labeled, but rather the whole area of the settlement, containing adjacent trees and surrounding meadows.

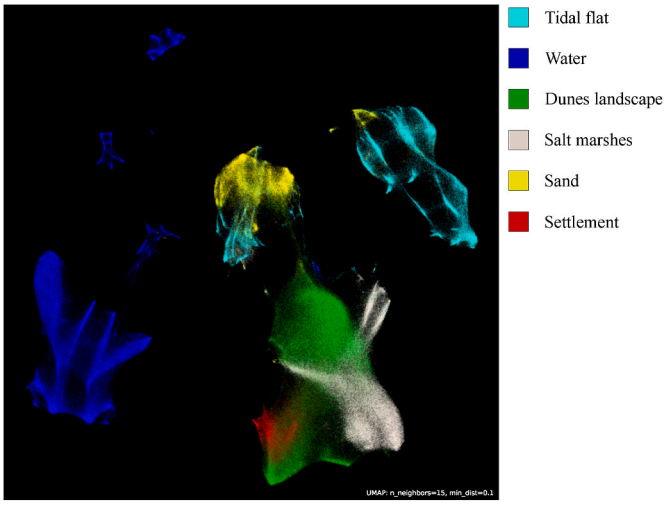

Fig. 5. UMAP projection of Pol-InSAR features. Projected data points are colored according to six generic land cover classes.

The resulting target class map, juxtaposed with the original biotope type map, is shown in Fig. 8.

2.2.3. Pol-InSAR-Island class map

Finally, the target class map is manually refined to optimally align the class labels based on the outdated biotope type map (2013) to reflect the current state of the more recent F-SAR acquisition (2022). The manual refinement is realized by visual interpretation of Pol-InSAR feature images and recent optical data. The optical data consulted for this purpose were acquired in an airborne survey one day after the F-SAR acquisition and have a ground resolution of 1 cm. Performing the highly time-consuming manual revision and validation of the labels is indispensable due to the large time difference between the generation of the biotope type map and the F-SAR acquisition. Fig. 9 shows the changes made to the target class map in this step to obtain the final, quality-assured Pol-InSAR-Island class map. For this purpose, both class maps are shown side by side (Fig. 9 (a) and (b)). In addition, Fig. 9 (c) and (d) highlight areas that have either been removed from the map, added, or replaced with another class. As expected, areas of the class *Sand*, which are highly exposed to sea disturbances, have undergone the most significant changes. A further notable aspect is the removal of several areas labeled as *Settlement* (red) in the target class map. This is due to the fact that in the Pol-InSAR-Island class map, only densely developed settlement areas were included, and open areas with very sparse built-up areas were not taken into account. In the area of *Salt marshes*, large-scale changes occur locally, as the boundary between the *Upper* and *Lower salt marsh* has changed over the years. For the remaining classes, primarily small-scale changes are evident. For example, the extent of *Coastal shrub* on the *Grey dune* has changed to a certain degree, and the area of the class *Peat bog* visible in the Pol-InSAR data has decreased in size due to increased vegetation cover. After the manual revision and

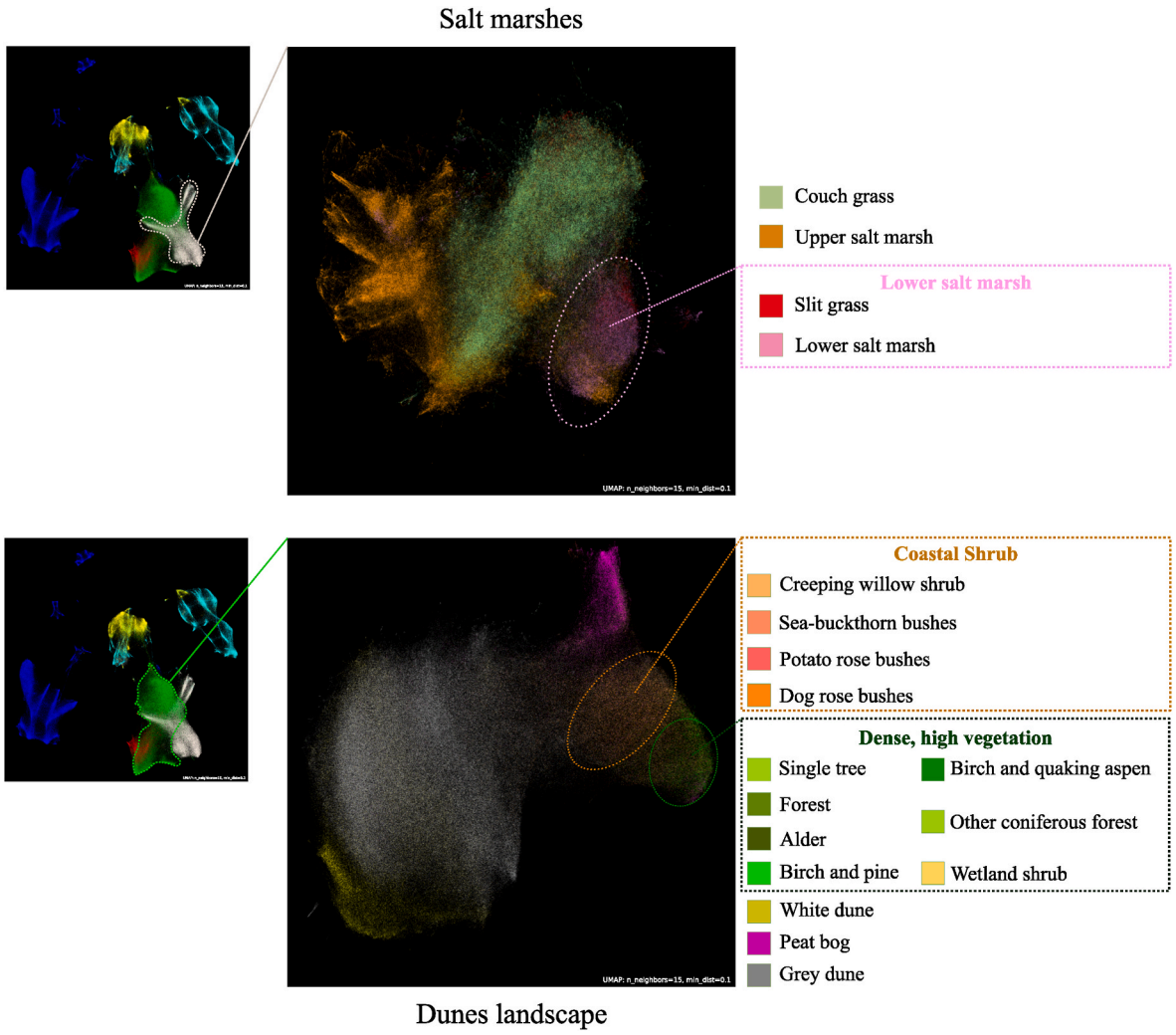

Fig. 6. Separability analysis of different biotope types, which belong to the generic class *Salt marshes* (top) and the generic class *Dunes landscape* (bottom), respectively.

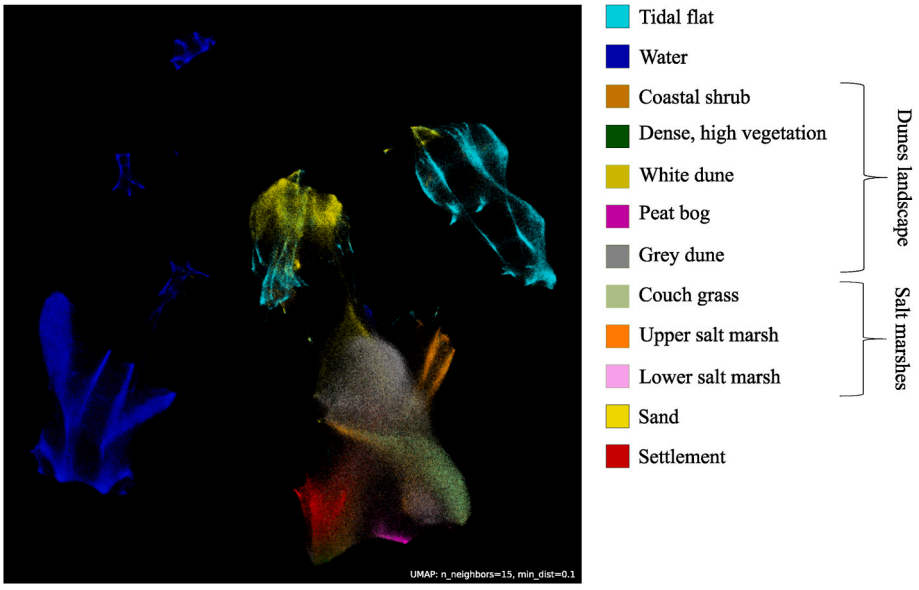

Fig. 7. UMAP projection of Pol-InSAR features. Projected data points are colored according to the 12 target classes of the Pol-InSAR-Island dataset.

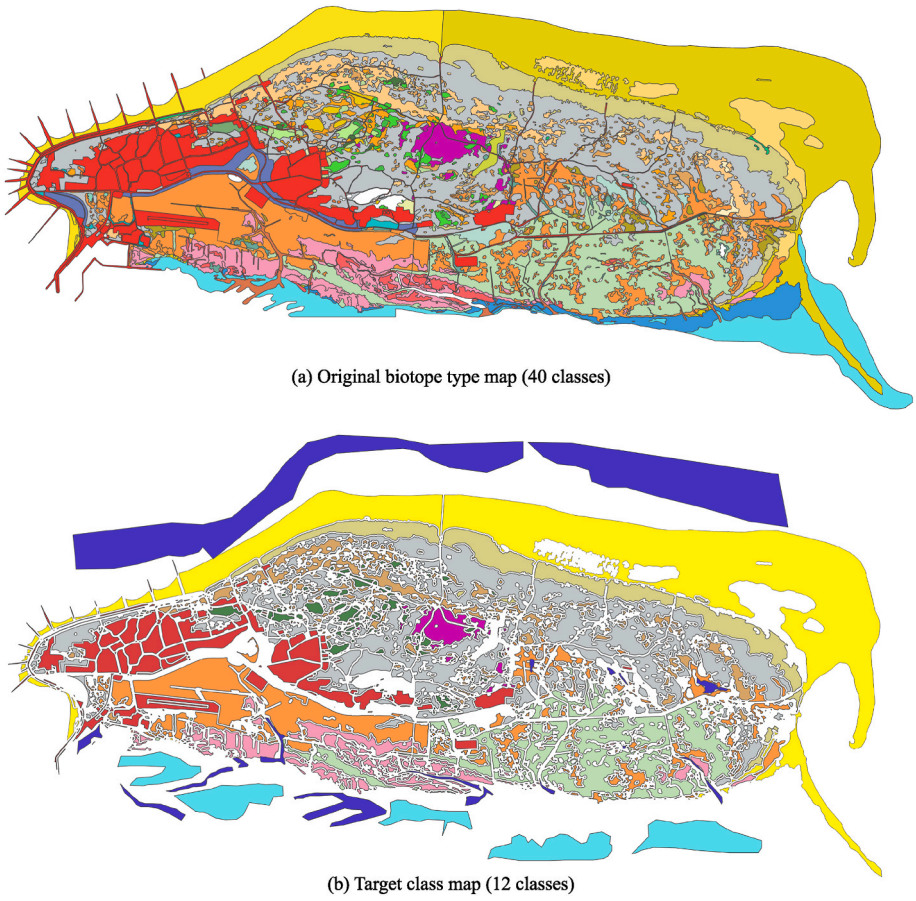

Fig. 8. Land cover maps for the island Baltrum. (a) shows the original biotope type map composed of 40 classes. (b) shows the target class map composed of 12 classes, which results after performing the steps *Manual Labeling (Water and Tidal flat)*, *Buffering & Filtering*, and *Merging of classes*. Corresponding legends can be found in Fig. 3 and 7.

validation of the labels, the final Pol-InSAR-Island class map is provided as part of the open benchmark dataset.

2.2.4. Training and test data split

The Pol-InSAR-Island dataset is divided into two spatially disjoint subsets for training and testing and, thus, for a fair comparison of different classification approaches. A chessboard grid is used for the partitioning, which alternately defines rectangular training and test regions with an extent of 512 m $\times$ 512 m each. This ensures that classes that are spatially concentrated on the island are adequately represented in both the training and the test set. In addition, this method of data splitting has the advantage that training and test samples are taken from the entire incidence angle interval ranging from 26 $^\circ$ to 58 $^\circ$. This is relevant because the incidence angle strongly influences the polarimetric backscatter signal, especially for surface scatterers such as *Sand*, *Water,* and *Tidal flat* ((Schmitz et al., 2022b)). It should be noted that the choice of spatially overlapping flight paths (see Fig. 1) results in an area that is doubly covered in the dataset. However, since the intersecting area was imaged from opposite flight directions, the SAR signatures vary between the two image sections. For this reason, both image sections of the intersecting area are retained in the dataset. In total, the dataset yields 2,677,248 labeled pixels for training and 2,773,559 for testing, distributed over the 12 target classes as listed in Table 2. As is typical for real-world data, the samples are not evenly distributed across the classes. The class imbalance complicates the task of land cover classification and needs to be addressed in the development of classifiers.

3. Baseline classifiers

Learning-based land cover classification of PolSAR data is a widely studied research topic for which many different approaches have been proposed, ranging from statistical methods ((Lee et al., 1994; Anfinsen et al., 2007)) to machine learning models based on polarimetric and hand-crafted texture features ((Fukuda and Hirosawa, 2001; Du et al., 2015)), to deep learning models ((Xie et al., 2014; Gao et al., 2017; Zhang et al., 2017)). In contrast, the use of multi-frequency Pol-InSAR data for land cover classification is significantly less addressed. However, a few studies demonstrate that incorporating interferometric or multi-frequency information into land cover classification approaches leads to improved classification performance ((Shimoni et al., 2009; Chen et al., 1996; Schmitz et al., 2022a; Ferro-Famil et al., 2002; Jin et al., 2014; Feng et al., 2017)). In the following, two commonly used learning-based models that allow the classification of (multi-frequency) Pol-InSAR data, namely a supervised Wishart classifier and a Random Forest classifier, are trained and tested on the presented Pol-InSAR-Island dataset. The obtained test results are intended to serve as minimum baselines for the Pol-InSAR-Island dataset for future work.

3.1. Supervised Wishart classifier

The Wishart classifier is one of the most prominent approaches to classify PolSAR data. It is a maximum likelihood classifier based on the complex Wishart distribution of the polarimetric coherency matrix ((Lee et al., 1994)). Since the polarimetric interferometric coherency matrix $\mathbf{T_6}$ is also Wishart distributed, the Wishart classifier can be adapted to Pol-InSAR data, as shown in (Lee et al., 2005). The classification can be

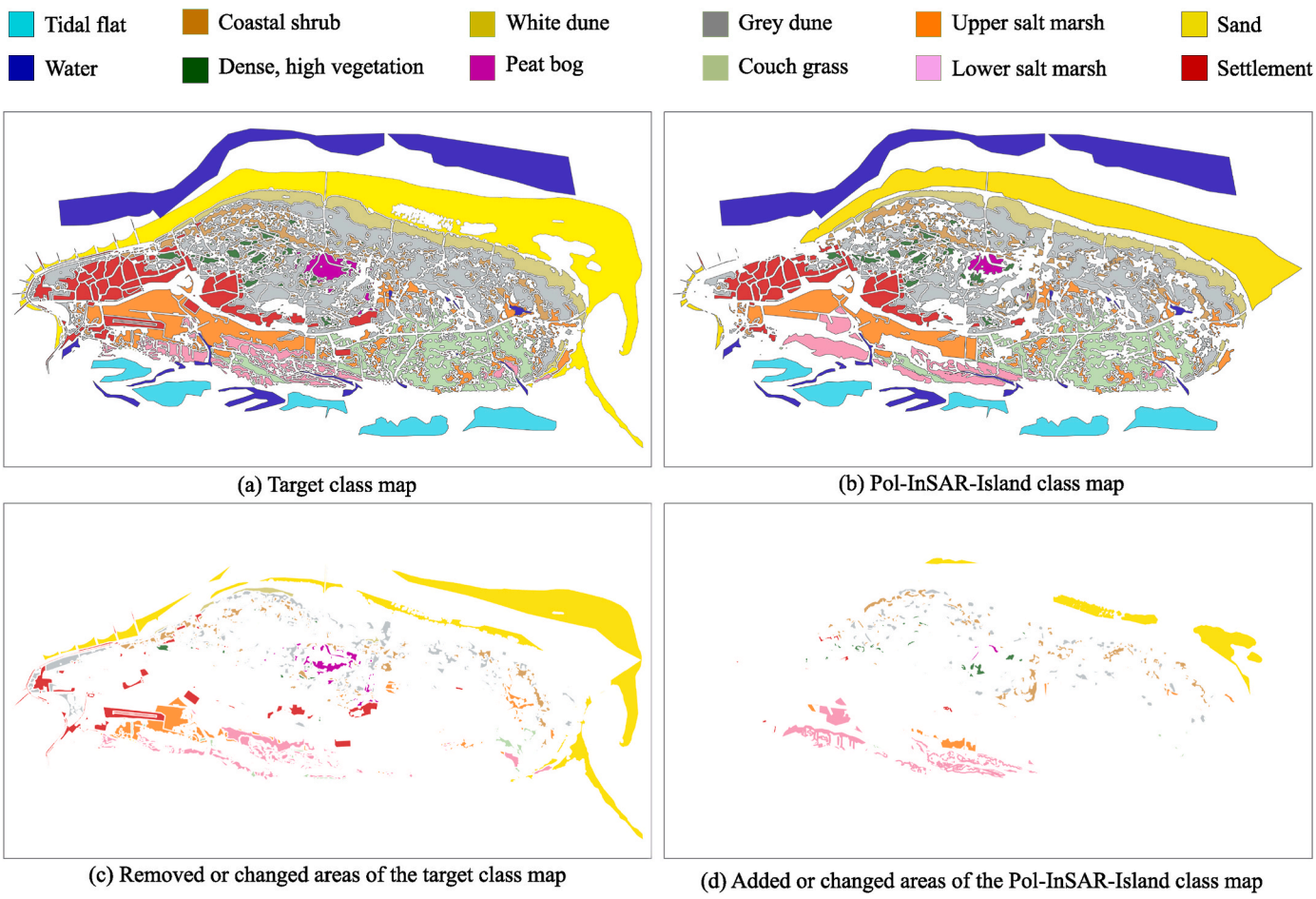

Fig. 9. Changes made to the target class map during manual refinement to obtain the final Pol-InSAR-Island class map. (a) shows the target class map, which serves as a starting point for the manual refinement. (b) shows the resulting Pol-InSAR-Island class map. (c) highlights areas that are removed from the map or assigned to a different class. These areas are colored according to their labels in the target class map. (d) highlights areas that are added to the map or assigned to a different class. These areas are colored according to their labels in the Pol-InSAR-Island class map.

Table 2
Percentage of labeled pixels per class contained in the training and the test set.

	TF	W	CS	DV	WD	PB	GD	CG	US	LS	S	SE
Training	7.09	17.98	5.29	2.04	6.72	0.87	17.78	8.17	8.01	5.85	14.92	5.28
Test	8.07	17.31	3.65	1.43	6.44	1.15	19.88	7.56	9.51	4.75	14.62	5.63

performed supervised, i.e., by including ground truth labels, or unsupervised by an initial clustering based on interferometric features, as proposed in (Ferro-Famil et al., 2006) and (Jager et al., 2007). Since ground truth labels are available from the Pol-InSAR-Island dataset, this paper only considers the supervised Wishart classification, which is performed separately for the L-band and S-band Pol-InSAR data. Prior to classification, the image data are spatially averaged using the Refined Lee filter with a window size of 9 × 9 pixels. Using all available training samples in the dataset, cluster centers, given by the mean coherency matrix of pixels labeled with the same target class, are determined. Subsequently, each pixel within the test regions is assigned to the target class corresponding to the nearest cluster center using a distance function based on the Wishart distribution.

3.2. Random Forest classifier

The Random Forest algorithm is a supervised ensemble learning method based on the combination of uncorrelated decision trees that has been widely used for the classification of PolSAR data ((Du et al., 2015; Loosvelt et al., 2012; Wang et al., 2017; Zhang et al., 2021)). Its successful application for Pol-InSAR classification is shown in (Jin et al., 2014). In this work, the Random Forest algorithm is applied to classify each image pixel of the Pol-InSAR-Island dataset based on feature vectors consisting of polarimetric and interferometric features listed in Table 1. After spatial averaging using the Refined Lee filter with a window size of 9 × 9 pixels, features are extracted from S- and L-band data using the PolSARpro software (Pottier et al., 2018). Random Forest models are trained using the Pol-InSAR-Island dataset to classify L-band and S-band data separately as well as combined. To select suitable hyperparameters, a 5-fold cross-validation is performed to estimate and compare expected classification performances of the model variations in terms of balanced accuracy. The relatively small number of 5 folds is assumed to be sufficient for robust estimation of classification performance due to the size of the dataset. The tested hyperparameters include the number of decision trees (100, 200, and 300) and the strategy for sample weighting (equal sample weighting and sample weighting inversely proportional to class frequencies). For each type of input data (S-band, L-band, S- & L-band), the highest estimated classification

performances are obtained using 300 decision trees and an equal weighting of samples. After fixing the hyperparameters, models are trained using the entire training data and tested on the held-out test data. For the implementation, the scikit-learn library is used (Pedregosa et al., 2011).

3.3. Results

Predicted class maps of the entire area of the Pol-InSAR-Island dataset, resulting from Wishart and Random Forest classifications, are visualized in Fig. 10. For the Wishart classification, where S- and L-band data are analyzed separately, many misclassifications are visible. In particular, the classes *Water* and *Tidal flat* are not correctly identified over the entire incidence angle interval. In general, the Random Forest classification performs better in this respect and also shows a better overall agreement with the Pol-InSAR-Island class map.

The quantitative results obtained on the held-out test data are summarized in Table 3. In order to compare the results in a concise way, two metrics that are commonly used for the evaluation of image segmentation are considered. These are mean IoU and balanced accuracy. The IoU, also known as Jaccard index (Jaccard, 1901), evaluates the overlap between the prediction and ground truth for one class i. It is defined as the ratio of the intersected to the combined area of prediction and ground truth:

$$\mathrm{IoU}_i = \frac{\text{Area of Intersection}}{\text{Area of Union}} = \frac{p_{ii}}{p_{ii} + p_{ji} + p_{ij}} \quad \text{with} \quad i \neq j \tag{3}$$

Here, p_{ii} denotes the number of pixels that are correctly predicted as class i, p_{ji} denotes the number of pixels that are incorrectly predicted as class i, and p_{ij} denotes the number of pixels that are part of class i in the ground truth mask but are not correctly predicted as class i. The mean IoU is given by the mean of all class-specific IoU scores, weighting all classes equally regardless of their size. The second metric, balanced accuracy, as defined in (Kelleher et al., 2020), is calculated by taking the average of recall (also known as sensitivity) for each class:

$$\text{balanced accuracy} = \frac{1}{k} \sum_{i=1}^{k} \frac{p_{ii}}{\sum_{j=1}^{k} p_{ij}}. \tag{4}$$

Here, k denotes the number of classes. Balanced accuracy is commonly used to evaluate classification results achieved on imbalanced test data because each class's performance equally contributes to the final score, irrespective of the class size.

The results of the Wishart classification with mean IoU scores of only 24.29 % (S-band) and 32.69 % (L-band) and balanced accuracy scores of 44.84 % (S-band) and 54.59 % (L-band) are significantly below the results of the Random Forest classification. As expected, the best result with a mean IoU of 67.00 % and balanced accuracy of 77.38 % is

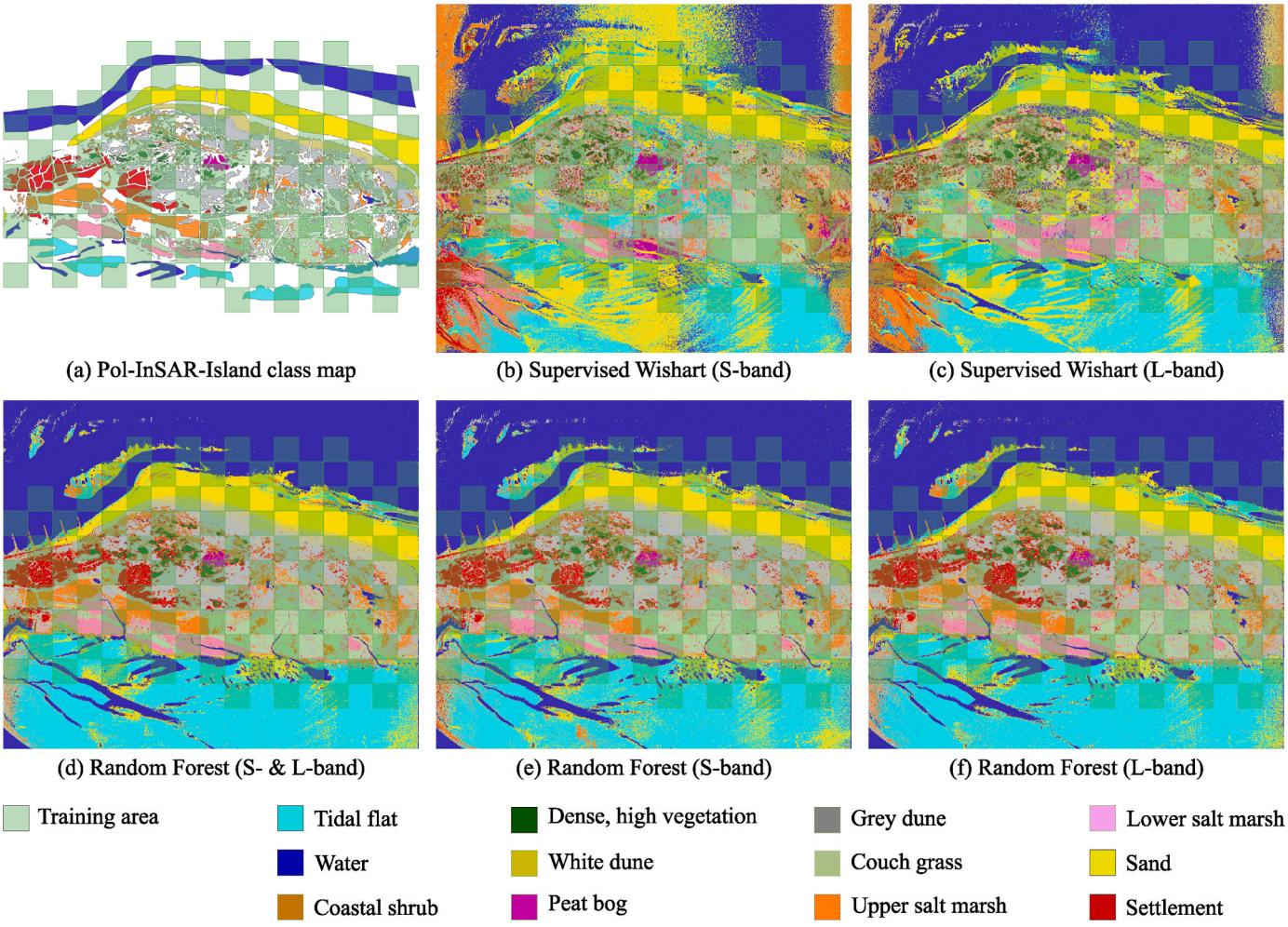

Fig. 10. Classification results of the entire dataset. Areas used for training are marked in green. (a) shows the Pol-InSAR-Island target class map, (b) the Wishart classification result based on S-band data, (c) the Wishart classification result based on L-band data, (d) the Random Forest classification based on S- & L-band data, (e) the Random Forest classification result based on S-band data and (f) the Random Forest classification result based on L-band data. (For interpretation of the references to color in this figure legend, the reader is referred to the Web version of this article.)

Table 3
Classification results given as class-wise IoU and recall as well as mean IoU and balanced accuracy (in %).

	TF	W	CS	DV	WD	PB	GD	CG	US	LS	S	SE	mean
Wishart, S-band													
IoU	30.42	42.19	16.35	22.31	9.17	26.64	17.16	39.31	7.76	19.50	44.57	16.13	24.29
recall	63.77	51.42	33.19	54.86	15.65	89.96	22.64	60.68	10.36	30.90	87.30	17.41	44.84
Wishart, L-band													
IoU	57.28	67.59	21.49	28.12	22.76	51.21	10.92	30.14	4.85	27.71	51.67	18.57	32.69
recall	81.95	82.02	46.81	63.72	37.12	88.96	12.26	63.98	5.52	61.16	91.73	19.89	54.59
Random Forest, S-band													
IoU	83.08	98.23	33.34	29.49	23.55	60.11	59.02	61.99	48.56	71.93	88.62	48.04	58.83
recall	91.64	99.26	56.25	37.29	28.30	66.57	82.71	82.27	56.16	87.37	95.04	60.44	70.28
Random Forest, L-band													
IoU	89.33	97.43	39.15	40.32	32.68	61.74	55.39	51.45	50.16	62.15	87.61	52.72	60.01
recall	92.32	98.93	61.25	53.82	43.95	66.81	75.88	70.63	58.68	81.09	94.64	67.19	72.10
Random Forest, S- and L-band													
IoU	91.13	98.98	42.94	45.13	41.09	68.97	63.37	65.27	59.18	78.26	91.77	57.93	67.00
recall	93.48	99.58	64.14	56.81	50.59	72.19	83.01	82.92	66.94	90.77	96.95	71.15	77.38

obtained by considering the S- and L-band together using the Random Forest classifier. However, the result still shows considerable room for improvement. As already indicated by the feature visualization in Fig. 7, the classification of the classes *Water*, *Tidal flat,* and *Sand* succeeds with high accuracy, while difficulties are encountered in the separation between *Coastal shrub* and *Dense, high vegetation*, which are characterized by similar polarimetric features. Since these two classes differ mainly in their vertical structure, improvements may be achieved by a more sophisticated inclusion of the interferometric data component. The class that is least recognized by the Random Forest classifier is *White dune*. The first row in Fig. 11 shows the ground truth and predicted class maps for a sample area capturing a *White dune*. It is apparent that particularly dense vegetated areas are falsely predicted as *Grey dune*. Reliable differentiation of the classes *White dune* and *Grey dune* will require the inclusion of spatial context information. Another observation is the incorrect prediction of the class *Settlement* in natural environments. This issue is shown exemplarily in Fig. 11 (d)–(f). Incorporating spatial image features into the classification could also lead to an improvement in this respect.

4. Discussion

The presented Pol-InSAR-Island dataset is the first open benchmark dataset for land cover classification of multi-frequency Pol-InSAR data, which is intended to advance the development of machine learning approaches in this field. The novelty lies in the public availability of such

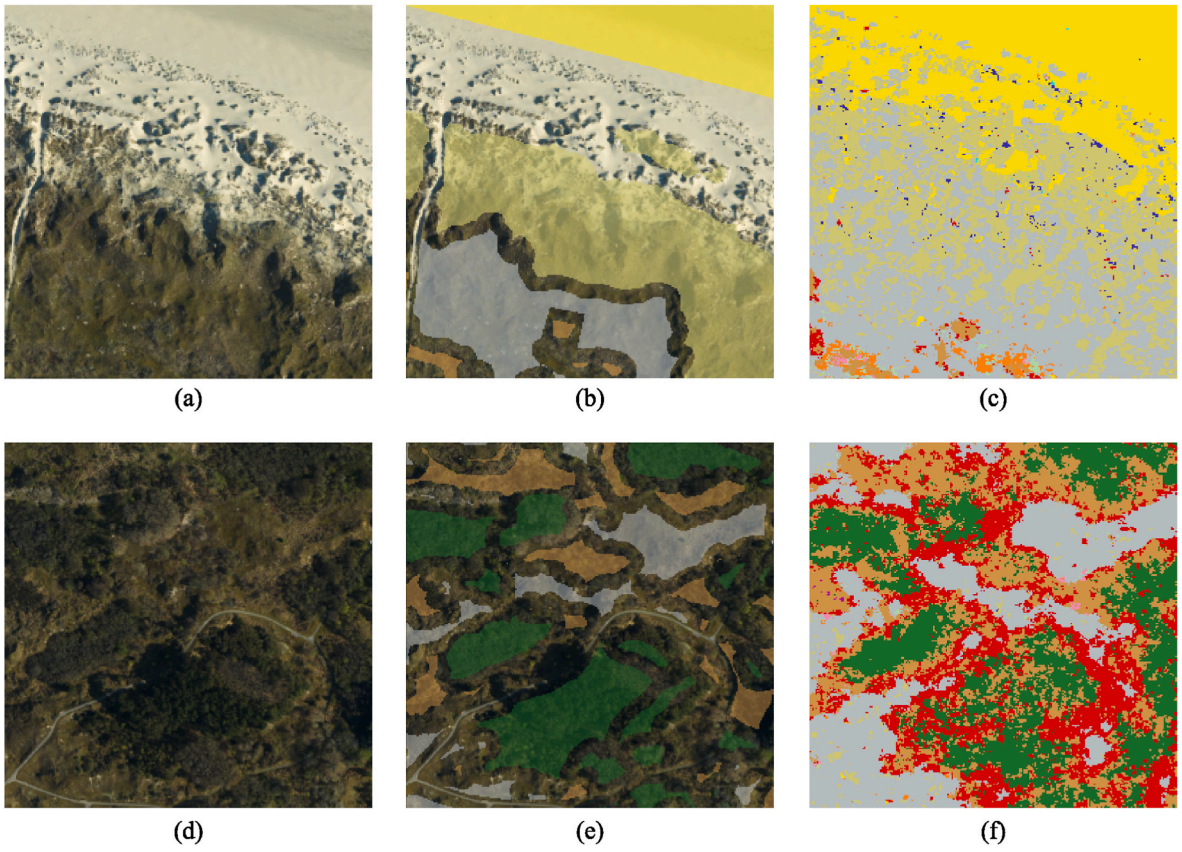

Fig. 11. Samples for typical classification errors of the Random Forest classification based on S- and L-band data. The first row ((a)–(c)) shows an area covered by the *White dune* class. The second row ((d)–(e)) shows an area covered by the classes *High, dense vegetation*, *Coastal shrub*, and *Grey dune*. Optical images are provided in (a) and (d), ground truth maps in (b) and (e), and Random Forest classification results in (c) and (f).

information-rich, high-resolution data products, as well as the corresponding well-designed class labels, which pose a challenging land cover classification task. As can be seen from the results of the two baseline approaches, the challenge of this task arises, on the one hand, from the low variance between classes, e.g., between *Coastal shrub* and *Dense, high vegetation*. On the other hand, the dataset contains target classes that are composed of different land covers (e.g., *White dune* and *Settlement*), thus requiring spatial context information to be learned and incorporated for correct classification. The first challenge can be tackled through the exploration and integration of sophisticated polarimetric and interferometric features. The second challenge can be effectively addressed by leveraging deep learning models to learn high-level spatial features. A synergistic combination of these approaches, incorporating pixel-based polarimetric and interferometric features and learned high-level spatial features, holds great promise and presents a highly sought-after research direction. The Pol-InSAR-Island benchmark dataset provides reliable training and test data that aims to encourage and enable researchers to develop and compare different machine learning approaches. The fixed definition of the training and test regions given in the dataset and the proposed evaluation metrics used in Section 3 ensure direct comparability of different approaches.

A limitation of the Pol-InSAR-Island dataset is the fragmentary labeling. In general, labeled areas of different target classes are not directly adjacent to each other but are separated by an unlabeled area. By employing machine learning methods, there is a risk of inaccurately detecting class boundaries and facing challenges in evaluating classifiers in this regard. Seamless labeling would, therefore, be desirable but is difficult or impossible to achieve with the available reference data. A further issue is the limited size of the dataset. The Pol-InSAR-Island dataset contains image data covering an area of about 15 km^2 with a ground resolution of 1 m $\times$ 1 m and more than 5 million labeled pixels in total. This exceeds the size of most existing datasets for PolSAR data classification but does not yet reach the size of datasets used in computer vision to train large deep learning models. In the future, it is conceivable to extend the dataset by incorporating additional data acquired during the F-SAR measurement campaign over the neighboring islands of Norderney and Langeoog. However, this requires a considerable time effort due to the manual improvement and validation of automatically generated labels, which is indispensable because of the time difference between the reference biotope type map and the SAR data acquisition. An extension of the dataset beyond the area of the East Frisian Islands is currently not planned. The main reason for this decision is the specific focus on typical local land cover classes, such as salt marshes and tidal flats, which have unique characteristics specific to the North Sea coast. Expanding the dataset with image data acquired from other SAR sensors (e.g., TerraSAR-X, RADARSAT-2, or Sentinel-1) also presents challenges. One major issue is the difficulty in directly matching the fine-scaled labels to lower spatial resolution data. Additionally, reliable adjustment and validation of labels become infeasible without additional (optical) reference data that have to be captured near the time of the SAR data acquisition. The limitation to a single sensor and a single location represents a weak point of the Pol-InSAR-Island dataset. As a result, classifiers trained on this dataset are unlikely to be transferable to other sensors and test sites without further adaptation. Thus, the main goal of providing this dataset is not to train universally applicable classifiers for practical use but rather to enable the development and comparison of novel multi-frequency Pol-InSAR data classification methods in a controlled training and test environment. The development of specialized classification approaches is crucial groundwork for upcoming spaceborne missions such as Biomass (Sedehi et al., 2021), which involves Pol-InSAR data acquisition in P-band, and NISAR (Kellogg et al., 2020), which will acquire Pol-InSAR data in S- and L-band.

Convenient access to the data is provided via KITopenData: https://doi.org/10.35097/1700. In order to reproduce the results of the baseline classifiers presented in this paper, the corresponding code is available on https://gitlab.kit.edu/sylvia.hochstuhl/pol_insar_island-baseline-classifiers.git. Users of this dataset are encouraged to evaluate the results of their own approaches with the metrics used in this paper.

5. Conclusion

In this paper, the first open multi-frequency Pol-InSAR benchmark dataset, named Pol-InSAR-Island, is presented to support the future development of machine learning methods for classifying land cover. The provision of this dataset addresses the urgent need for reliable and comprehensive training data, especially for the application and adaption of recent machine learning methods to multi-frequency Pol-InSAR data. The investigation of such methods in a controlled training and test environment plays an important role, especially with respect to future multi-frequency Pol-InSAR spaceborne missions.

In order to provide all users of the dataset with detailed background information regarding the generation of class labels, the process of semi-automatic generation of class labels was presented in detail in this paper. The main focus was on the selection of suitable target classes, which is performed by a visual class separability analysis based on polarimetric and interferometric features. Additionally, two established classification methods – a supervised Wishart classifier and a Random Forest classifier, which serve as a minimal baseline, are trained and tested on the Pol-InSAR-Island dataset. The obtained mean IoU of a maximum of 67% and balanced accuracy of a maximum of 77% indicate the challenge of the given task. These values leave room for improvement through the implementation of more sophisticated classifiers. Currently, the extension of the dataset with F-SAR data acquired over Norderney and Langeoog has not been accomplished due to the substantial time needed for manual refinement and label validation. Nevertheless, this remains a potential avenue for future endeavors.

Disclosure of the use of AI-assisted technology in the writing process

During the preparation of this work, the authors used DeepL (Write) in order to rephrase selected sentences written by the authors themselves. After using this tool, the authors reviewed and edited the content as needed and take full responsibility for the content of the publication.

Declaration of competing interest

The authors declare that they have no known competing financial interests or personal relationships that could have appeared to influence the work reported in this paper.

Acknowledgement

We acknowledge support by the KIT-Publication Fund of the Karlsruhe Institute of Technology.

References

Anfinsen, S.N., Jenssen, R., Eltoft, T., 2007. Spectral clustering of polarimetric SAR data with Wishart-derived distance measures. In: POLinSAR, 7, pp. 1–9.
Cao, Y., Wu, Y., Li, M., Zheng, M., Zhang, P., Wang, J., 2023. Multifrequency PolSAR image fusion classification based on semantic interactive information and topological structure. IEEE Trans. Geosci. Rem. Sens. 61, 1–15.
Chen, K., Huang, W., Tsay, D., Amar, F., 1996. Classification of multifrequency polarimetric SAR imagery using a dynamic learning neural network. IEEE Trans. Geosci. Rem. Sens. 34 (3), 814–820.
Cloude, S., Papathanassiou, K., 1998. Polarimetric SAR interferometry. IEEE Trans. Geosci. Rem. Sens. 36 (5), 1551–1565.
Cloude, S., Pottier, E., 1997. An entropy based classification scheme for land applications of polarimetric SAR. IEEE Trans. Geosci. Rem. Sens. 35 (1), 68–78.
Cordts, M., Omran, M., Ramos, S., Rehfeld, T., Enzweiler, M., Benenson, R., Franke, U., Roth, S., Schiele, B., 2016. The cityscapes dataset for semantic urban scene understanding. In: Proceedings of the IEEE Conference on Computer Vision and Pattern Recognition, pp. 3213–3223.

De, S., Ratha, D., Ratha, D., Bhattacharya, A., Chaudhuri, S., 2018. Tensorization of multifrequency PolSAR data for classification using an autoencoder network. Geosci. Rem. Sens. Lett. IEEE 15 (4), 542–546.
Deng, J., Dong, W., Socher, R., Li, L.-J., Li, K., Fei-Fei, L., 2009. ImageNet: a large-scale hierarchical image database. In: Proceedings of the IEEE Conference on Computer Vision and Pattern Recognition, pp. 248–255.
Du, P., Samat, A., Waske, B., Liu, S., Li, Z., 2015. Random Forest and Rotation Forest for fully polarized SAR image classification using polarimetric and spatial features. ISPRS J. Photogrammetry Remote Sens. 105, 38–53.
Feng, Q., Zhou, L., Chen, E., Liang, X., Zhao, L., Zhou, Y., 2017. The performance of airborne C-band PolInSAR data on forest growth stage types classification. Rem. Sens. 9 (9), 955.
Ferro-Famil, L., Pottier, E., Lee, J., 2002. Classification and interpretation of polarimetric interferometric SAR data. In: IEEE International Geoscience and Remote Sensing Symposium, 1, pp. 635–637.
Ferro-Famil, L., Kugler, F., Potier, E., Lee, J.-S., 2006. Forest mapping and classification at L-band using pol-InSAR optimal coherence set statistics. In: European Conference on Synthetic Aperture Radar, pp. 1–4.
Fukuda, S., Hirosawa, H., 2001. Support vector machine classification of land cover: application to polarimetric SAR data. In: 2001 IEEE International Geoscience and Remote Sensing Symposium, 1, pp. 187–189.
Gao, F., Huang, T., Wang, J., Sun, J., Hussain, A., Yang, E., 2017. Dual-branch deep convolution neural network for polarimetric SAR image classification. Appl. Sci. 7 (5), 447.
Horn, R., Nottensteiner, A., Reigber, A., Fischer, J., Scheiber, R., 2009. F-SAR — DLR's new multifrequency polarimetric airborne SAR. In: 2009 IEEE International Geoscience and Remote Sensing Symposium, 2. II–902–II–905.
Jaccard, P., 1901. Distribution de la flore alpine dans le bassin des dranses et dans quelques régions voisines. Bull. Soc. Vaudoise Sci. Nat. 37, 241–272.
Jager, M., Neumann, M., Guillaso, S., Reigber, A., 2007. A self-initializing PolInSAR classifier using interferometric phase differences. IEEE Trans. Geosci. Rem. Sens. 45 (11), 3503–3518.
Jin, H., Mountrakis, G., Stehman, S.V., 2014. Assessing integration of intensity, polarimetric scattering, interferometric coherence and spatial texture metrics in PALSAR-derived land cover classification. ISPRS J. Photogrammetry Remote Sens. 98, 70–84.
Kelleher, J.D., Mac Namee, B., D'arcy, A., 2020. Fundamentals of Machine Learning for Predictive Data Analytics: Algorithms, Worked Examples, and Case Studies. MIT press.
Kellogg, K., Hoffman, P., Standley, S., Shaffer, S., Rosen, P., Edelstein, W., Dunn, C., Baker, C., Barela, P., Shen, Y., et al., 2020. NASA-ISRO synthetic aperture radar (NISAR) mission. In: 2020 IEEE Aerospace Conference, IEEE, pp. 1–21.
Lee, J.S., Grunes, M.R., Kwok, R., 1994. Classification of multi-look polarimetric SAR imagery based on complex Wishart distribution. Int. J. Rem. Sens. 15 (11), 2299–2311.
Lee, J., Papathanassiou, K., Hajnsek, I., Mette, T., Grunes, M., Ainsworth, T., Ferro-Famil, L., 2005a. Applying polarimetric SAR interferometric data for forest classification. In: 2005 IEEE International Geoscience and Remote Sensing Symposium, 7, pp. 4848–4851. Seoul Korea.
Lee, J.S., Grunes, M., Ainsworth, T.L., Hajnsek, I., Mette, T., Papathanassiou, K., 2005b. Forest Classification Based on L-Band Polarimetric and Interferometric SAR Data, 586. ESA Special Publication, p. 6.
X. Liu, L. Jiao, F. Liu, PolSF: PolSAR Image Dataset on San Francisco, arXiv:1912.07259 [cs, eess].
Loosvelt, L., Peters, J., Skriver, H., De Baets, B., Verhoest, N.E.C., 2012. Impact of reducing polarimetric SAR input on the uncertainty of crop classifications based on the random forests algorithm. IEEE Trans. Geosci. Rem. Sens. 50 (10), 4185–4200.
L. McInnes, J. Healy, J. Melville, Umap: Uniform Manifold Approximation and Projection for Dimension Reduction, arXiv preprint arXiv:1802.03426.
Mohammadimanesh, F., Salehi, B., Mahdianpari, M., Gill, E., Molinier, M., 2019. A new fully convolutional neural network for semantic segmentation of polarimetric SAR imagery in complex land cover ecosystem. ISPRS J. Photogrammetry Remote Sens. 151, 223–236.
Newman, L., Weissgerber, F., Plyer, A., Colin, E., 2023. Advantages of polarimetry and interferometry for semantic segmentation of urban SAR images with consideration of the layover. In: 2023 Joint Urban Remote Sensing Event. JURSE), pp. 1–4.
Parikh, H., Patel, S., Patel, V., 2020. Classification of SAR and PolSAR images using deep learning: a review. International Journal of Image and Data Fusion 11 (1), 1–32.
Pedregosa, F., Varoquaux, G., Gramfort, A., Michel, V., Thirion, B., Grisel, O., Blondel, M., Prettenhofer, P., Weiss, R., Dubourg, V., Vanderplas, J., Passos, A., Cournapeau, D., Brucher, M., Perrot, M., Duchesnay, E., 2011. Scikit-learn: machine learning in Python. J. Mach. Learn. Res. 12 (85), 2825–2830.
Pinheiro, M., Amao-Oliva, J., Scheiber, R., Jaeger, M., Horn, R., Keller, M., Fischer, J., Reigber, A., 2020. Dual-frequency airborne SAR for large scale mapping of tidal flats. Rem. Sens. 12 (11), 1827.
Pinheiro, M., Scheiber, R., Amao-Oliva, J., Jaeger, M., Horn, R., Fischer, J., Keller, M., Reigber, A., 2021. Airborne SAR interferometry for large scale mapping of tidal flats: the GeoWAM project. In: 13th European Conference on Synthetic Aperture Radar, pp. 1–6.
Pottier, E., Ferro-Famil, L., Fitrzyk, M., Desnos, Y.-L., 2018. PolSARpro-BIO: the new scientific toolbox for ESA & third party fully polarimetric SAR missions. In: 12th European Conference on Synthetic Aperture Radar, pp. 1–4.
Praks, J., Koeniguer, E.C., Hallikainen, M.T., 2009. Alternatives to target entropy and alpha angle in SAR polarimetry. IEEE Trans. Geosci. Rem. Sens. 47 (7), 2262–2274.
Schmitz, S., Weinmann, M., Thiele, A., 2020. Incorporating interferometric coherence into LULC classification of airborne PolSAR-images using fully convolutional networks. In: The International Archives of the Photogrammetry, Remote Sensing and Spatial Information Sciences, XLIII-B1-2020, pp. 115–122.
Schmitz, S., Hammer, H., Thiele, A., 2022a. Multi-frequency PolInSAR data are advantageous for land cover classification – a visual and quantitative analysis. In: ISPRS Annals of the Photogrammetry, Remote Sensing and Spatial Information Sciences, V-1-2022, pp. 49–56.
Schmitz, S., Thiele, A., Hammer, H., Hinz, S., 2022b. Impact of highly varying incidence angle on the feature space of PolSAR images. In: 14th European Conference on Synthetic Aperture Radar, pp. 1–6.
Sedehi, M., Carbone, A., Imbembo, E., Heliere, F., Rommen, B., Fehringer, M., Scipal, K., Leanza, A., Simon, T., Willemsen, P., 2021. Biomass-A fully polarimetric P-band SAR ESA mission. In: EUSAR 2021; 13th European Conference on Synthetic Aperture Radar. VDE, pp. 1–5.
Shimoni, M., Borghys, D., Heremans, R., Perneel, C., Acheroy, M., 2009. Fusion of PolSAR and PolInSAR data for land cover classification. Int. J. Appl. Earth Obs. Geoinf. 11 (3), 169–180.
Truong-Loi, M.-L., Freeman, A., Dubois-Fernandez, P.C., Pottier, E., 2009. Estimation of soil moisture and faraday rotation from bare surfaces using compact polarimetry. IEEE Trans. Geosci. Rem. Sens. 47 (11), 3608–3615.
Turkar, V., Deo, R., Rao, Y.S., Mohan, S., Das, A., 2012. Classification Accuracy of Multi-Frequency and Multi-Polarization SAR images for various land covers. IEEE J. Sel. Top. Appl. Earth Obs. Rem. Sens. 5 (3), 936–941.
Vissers, M.a.M., Sanden, J.J.v. d., 1992. Groundtruth collection for the JPL-SAR and ERS-1 campaign in Flevoland and the veluwe (NL) 1991. Tech. Rep. 31.
Wang, X., Wang, H., 2019. Forest height mapping using complex-valued convolutional neural network. IEEE Access 7, 126334–126343.
Wang, W., Yang, X., Li, X., Chen, K., Liu, G., Li, Z., Gade, M., 2017. A fully polarimetric SAR imagery classification scheme for mud and Sand flats in intertidal zones. IEEE Trans. Geosci. Rem. Sens. 55 (3), 1734–1742.
Wang, Z., Zeng, X., Yan, Z., Kang, J., Sun, X., 2022. AIR-PolSAR-seg: a large-scale data set for terrain segmentation in complex-scene PolSAR images. IEEE J. Sel. Top. Appl. Earth Obs. Rem. Sens. 15, 3830–3841.
Xie, H., Wang, S., Liu, K., Lin, S., Hou, B., 2014. Multilayer feature learning for polarimetric synthetic radar data classification. In: 2014 IEEE Geoscience and Remote Sensing Symposium, pp. 2818–2821.
Xin, X., Li, M., Wu, Y., Zheng, M., Zhang, P., Xu, D., Wang, J., 2022. Semi-supervised classification of dual-frequency PolSAR image using joint feature learning and cross label-information network. IEEE Trans. Geosci. Rem. Sens. 60, 1–16.
Yamaguchi, Y., Yajima, Y., Yamada, H., 2006. A four-component decomposition of POLSAR images based on the coherency matrix. Geosci. Rem. Sens. Lett. IEEE 3 (3), 292–296.
Zhang, Z., Wang, H., Xu, F., Jin, Y.-Q., 2017. Complex-valued convolutional neural network and its application in polarimetric SAR image classification. IEEE Trans. Geosci. Rem. Sens. 55 (12), 7177–7188.
Zhang, X., Xu, J., Chen, Y., Xu, K., Wang, D., 2021. Coastal wetland classification with GF-3 polarimetric SAR imagery by using object-oriented random forest algorithm. Sensors 21 (10), 3395.
Zhu, X.X., Montazeri, S., Ali, M., Hua, Y., Wang, Y., Mou, L., Shi, Y., Xu, F., Bamler, R., 2021. Deep learning meets SAR: concepts, models, pitfalls, and perspectives. IEEE Geoscience and Remote Sensing Magazine 9 (4), 143–172.